An ultra-compact shortwave infrared hyperspectral imaging system

Jay Giblin[1], Rusha Chatterjee[1*], Michael Chase[1], Michael Ascenzi[1], Jonathan Rameau[1], Julia Dupuis[1], Jacob A. Martin[2], and Joseph Meola[2]
[1]Physical Sciences Inc., Andover MA
[2]Air Force Research Laboratory, 2241 Avionics Circle, Wright-Patterson Air Force Base

ABSTRACT

Physical Sciences Inc. has developed an ultra-compact shortwave infrared (SWIR) staring mode hyperspectral imaging (HSI) sensor with an additional visible full motion video (FMV) capability. The innovative HSI design implements a programmable micro-electromechanical system entrance slit that breaks the interdependence between vehicle speed, frame rate, and spatial resolution of conventional push-broom systems and enables staring-mode operation without cooperative motion of the host vehicle or aircraft. The FMV and HSI components fit within 1000 cm^3, weigh a total of 2.1 lbs., and draw 15 W of power. The sensor mechanical design is compatible with gimbal-based deployment allowing for easy integration into ground vehicles or aircrafts. The FMV is capable of achieving NIRS-6 imagery over a 6°×6° field-of-view (FOV) at a 1500 ft. standoff. The SWIR HSI covers a spectral range of 900-1605 nm with a 15 nm spectral resolution, and interrogates a 5°×5° FOV per 1.6 s with a 2.18 mrad instantaneous FOV (1 m ground sample distance at 1500 ft.). A series of outdoor tests at standoffs up to 300 ft. have been conducted that demonstrate the payload's capability to acquire HSI information. The payload has direct utility towards diverse remote sensing applications such as vegetation monitoring, geological mapping, surveillance, etc. The data product utility is demonstrated through the spectral identification of materials (e.g. foam and cloth) placed in the sensor's FOV.

Keywords: Hyperspectral Imaging, Shortwave Infrared, Full Motion Video

1. INTRODUCTION

Physical Sciences Inc. (PSI) has developed a shortwave infrared (SWIR) hyperspectral imaging (HSI) sensor equipped with visible full motion video (FMV). The HSI/FMV technology offers broadband HSI performance in an ultra-compact, staring mode sensor. The sensor is capable of acquiring hyperspectral imagery across the SWIR 1 (900 – 1600 nm) band. The design is compatible with small gimbal-based deployment with all components fitting within 1000 cm^3, making it well aligned for diverse remote sensing applications such as vegetation monitoring, geospatial characterization, and intelligence surveillance and reconnaissance from ground based or aerial host platforms.

The HSI/FMV sensor leverages two critical technology components:

- The first component is a SWIR HSI sub-system based on a compact Czerny-Turner style spectrometer coupled with a digital micromirror device (DMD) that functions as an agile programmable entrance slit.
- The second component is a compact, board level, mega-pixel CMOS color imager with a fixed focal length imaging optic.

The sensor concept is illustrated in Figure 1a. Incoming light from the scene is imaged onto the DMD. A programmable slit is scanned across the imaged scene by sequentially actuating a strip of DMD mirrors into the on-state. Reflected light from the entrance slit is collimated and directed to a diffraction grating. The diffraction grating disperses spectral information from each mirror element along the vertical dimension of the slit. The spectral and spatial information is imaged onto an InGaAs focal plane array (FPA). Frames are synchronously acquired while the DMD scans the slit over the imaged scene to build up the full hyperspectral cube (Figure 1b). Critically, the DMD-based spectrometer slit breaks the interdependence between aircraft speed, frame rate, and spatial resolution of conventional push-broom HSI systems and enables staring-mode operation, flexible revisit, and/or foveation over a region of interest without requiring cooperative motion of the host platform. An industrial Nvidia TX2 single board computer (SBC) within the sensor housing synchronizes measurements, constructs data cubes, and executes automated target detection algorithms.

*Corresponding author: rchatterjee@psicorp.com

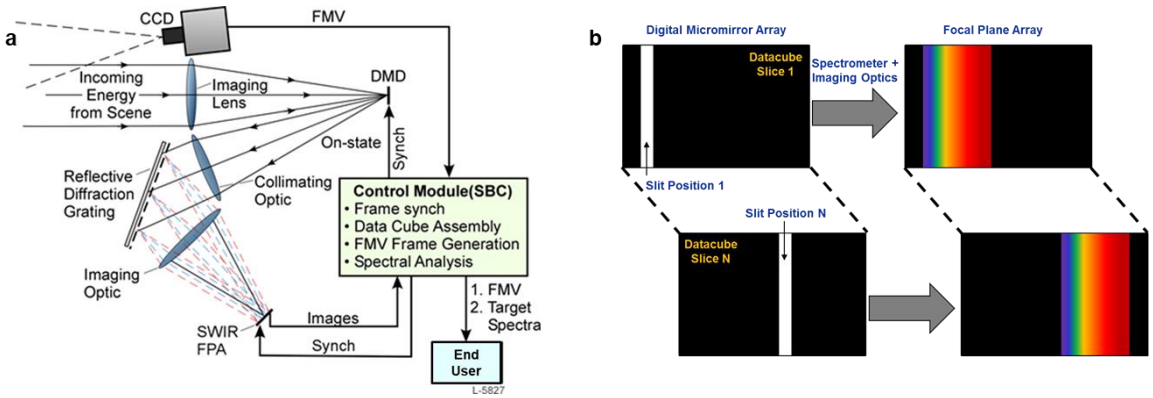

Figure 1: (a) Illustration of the HSI/HMV sensor concept. (b) A conceptual schematic of DMD entrance slits mapping to the FPA.

The FMV achieves images a 6°×6° field-of-view (FOV) with an instantaneous FOV (IFOV) of 1.1 mrad and NIRS-6 imaging performance at a 1500 ft. standoff. The SWIR HSI is boresighted with the FMV channel and covers a spectral range of 900-1605 nm with <12 nm spectral resolution, and acquires hyperspectral imagery across a 5°×5° FOV per 1.6 s with a 2.18 mrad instantaneous FOV. The sensor outputs radiometrically calibrated SWIR hyperspectral cubes with a 40×40 (spatial) × 95 (spectral) in a band sequential format, with associated visible FMV imagery at 25.6 Hz.

In this work, we discuss the overall sensor design and describe its characterization, as well as demonstrate its performance towards target detection applications. Specifically, Section 2 describes the sensor's opto-mechanical design and data acquisition and processing flow. Characterization of the sensor's optical performance metrics such as spatial resolution, spectral resolution, smile and keystone in hyperspectral imagery, and HSI sensitivity are presented in Section 3. The performance and utility of the sensor for applications such as spectral correlation based target detection is demonstrated in Section 4.

2. SENSOR DESIGN

2.1 Optical design

Figure 2 shows the optical layout of the HSI/FMV sensor. The sensor comprises a Czerny-Turner HSI spectrometer, boresighted with the FMV sub-system through a dichroic beamsplitter. The HSI system has a compact ~75 × 25 × 15 mm^3 footprint, compatible with the size constraints of a small gimbal payload. The sensor is designed to align all optical elements within the same plane. Doing so enables the spectrometer and visible imaging components to mount on a common central scaffolding plate.

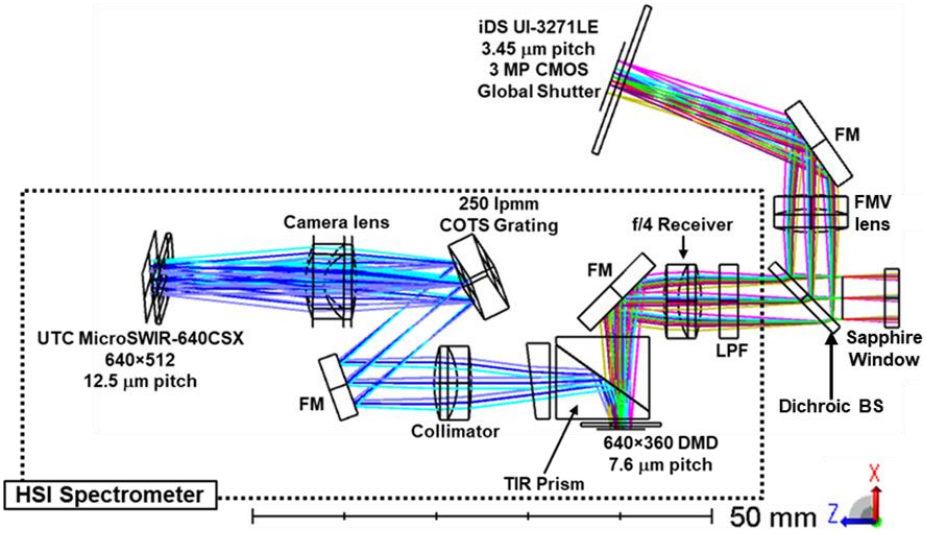

Figure 2: Optical design of the HSI/FMV sensor.

A 785 nm dichroic beamsplitter (Semrock) is placed prior to the spectrometer's receiver optic. The use of the beamsplitter enables the sensor's FMV camera to be boresighted with the HSI FOV. An 850 nm long pass filter (Semrock) is placed after the beamsplitter and prior to the receiver optic of the spectrometer. The long pass filter is used to mitigate order confusion from m = 2 wavelengths (425–850 nm) and m = 3 wavelengths (< 425 nm).

An f/4 achromatic doublet, placed after the beamsplitter, images a 5°×5° scene onto the system's programmable DMD slit. The DMD is a small form factor DLP-DLCR2000-EVM module from Texas Instruments [controlled using a customized low profile BeagleBone Black (BBB) host processor (Avnet)]. The module is based on the 640×360 resolution DLP2000 .2nHD DMD chipset with a 7.6 μm pixel pitch. 5×5 binning on the DMD results in an effective 38 μm slit width. A second f/4 achromatic doublet collimates light from the DMD onto a commercially available 250 lpmm grating (Richardson Gratings). A third f/4 achromatic doublet is used to form an image of the dispersed DMD slit onto an InGaAs FPA (Micro-SWIR 640CSX from UTC Sensors Unlimited coupled with an EPIX EB1mini mPCIe frame grabber). The FPA has a 640×512 pixel format with a 12.5 μm pixel pitch. A 25 ms integration is used to acquire HSI images per slit and 3×3 FPA pixels are binned in post processing. The combination of the DMD/FPA binning and the integration time allows for achievement of high signal-to-noise ratios (SNRs) against typically expected spectral radiances on the sensor (discussed in Section 3).

2.2 Control flow and data processing

The control flow block diagram of the HSI/FMV sensor is shown in Figure 3. Specifically, a TX2/Elroy SBC forms the main control unit of the HSI/FMV system. The SBC initializes sub-systems, initiates acquisition, processes frames and transmits data cubes. Upon initiating an acquisition, the TX2 triggers the BBB control unit to initiate mask loading. The BBB forms a sub-control unit and controls the DMD driver board, and handles acquisition triggering and synchronization with slit images. The BBB has slit images (masks) stored in memory which are transferred sequentially to the DMD controller and subsequently loaded onto the micromirror array. The BBB/DMD cycles through 41 mask images for each data cube where:

- Mask 1: Background frame (no slit, all DMD mirrors in off-state)
- Mask 2-41: Slit images

The SWIR and visible cameras are triggered synchronously with the mask loading.

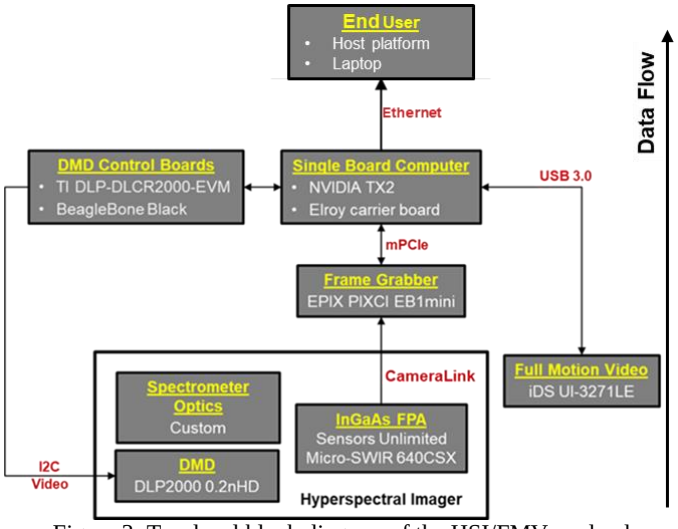

Figure 3: Top-level block diagram of the HSI/FMV payload highlighting the primary system components.

The acquired images are transferred to the SBC for processing. The HSI data cube processing includes the following:

- Background frame subtraction from raw slit frames.
- Wavelength calibration: Here each co-added and binned slit frame is resampled to a common wavelength-column calibration spanning the 900 – 1605 nm spectral range across 95 pixels (7.5 nm/pixel). This step accounts for the varying dispersion across spectrometer slit-position and eliminates the need for a slit-wise calibration curve in the processed cube.
- Rotation correction: In this step, each column is cropped down to the slit-width (in pixels) starting at pre-determined row indices to correct for the overall rotation of the HSI image (discussed in Section 3).
- Radiometric calibration for each corrected slit image, where calibration arrays are pre-loaded onto the SBC.

The processed and radiometrically calibrated slit images are appended to a final data cube which is then reshaped into a band sequential format with dimensions of 44 × 40 (spatial) × 95 (spectral) pixels. The system currently uses a direct Ethernet connection to access the SBC, control the sensor, and acquire and transfer data to the end-user's computer.

2.3 Mechanical design

The HSI/FMV system has been designed to be compatible with a commercially available 5" gimbal platform (Ascendant Engineering Solutions, AES). Figure 4 shows 3D solid models of the sensor exterior integrated with the gimbal platform and the sensor interior with key system components. The sensor consists of two ribbed annular shells mounted to a common central scaffold. All system components are mounted on either sides of the central scaffold and enclosed within the outer shells. The sensor stiffness allows maintenance of stabilized gimbal motion with the first structural mode at ≥120Hz. The ribbed shell design enables sensor performance at high ambient temperatures while simultaneously maintaining stiffness requirements. Specifically, the design enables maintenance of all system components within their operating temperature in an ambient 50° C environment (assuming a 5 knot wind speed).

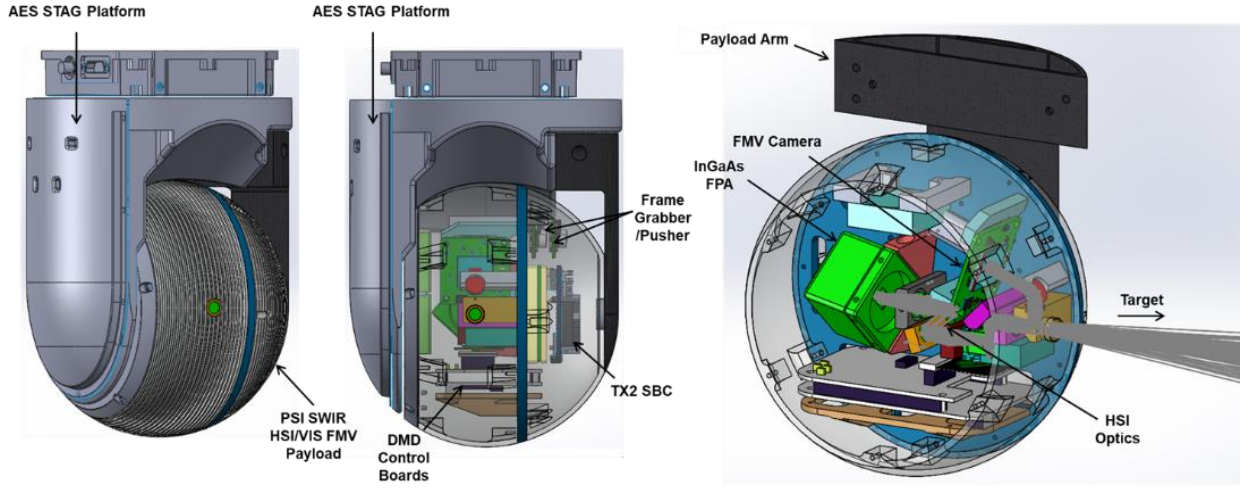

Figure 4: 3D solid model of the HSI sensor (left) integrated with the gimbal platform and (middle, right) interior with key components indicated.

3. SENSOR CHARACTERIZATION

3.1 Size, weight and power

Figure 5 shows photographs of the fully assembled sensor with opto-mechanics and electronics mounted to the central scaffolding and enclosed in the annular shells. The sensor has two external wires for power and Ethernet (for user control). The cover plate has a central ¼-20 tapped hole that can be used to mount the sensor on a tripod or a post. All the FMV and HSI components fit within 1000 cm^3, with the fully assembled system weighing 2.1 lbs. The sensor consumes < 20 W at max power draw during data acquisition. The size, weight and power (SWaP) metrics are outlined in Table 1.

Table 1: Payload SWaP.

Metric	Value
Size	1000 cm^3 (5.36 in. diameter)
Weight	2.1 lbs.
Power	Idle: 10 W (average); 11 W (peak) Acquisition: 15 W (average); 16 W (peak)

3.2 FMV spatial resolution

The FMV spatial resolution was characterized by acquiring images of standard AF tri-bar targets. Figure 6a and b show the FMV-acquired image of a USAF 1951 tri-bar target. Figure 6c shows the modulation transfer function (MTF), extracted from the images of the -2, -1, 0 and 1 groups of the target (solid green circles) plotted against the equivalent ground resolved distance (GRD) at 1500 ft. Associated tri-bar target spatial frequencies are indicated on the upper x-axis. The dashed black line represents the diffraction limit and the solid vertical line indicates the system's Nyquist limit. The plot shows that MTFs > 0.5 are observed for GRD > 0.4 m/lp. Additionally, MTFs ranging from 0.2 to 0.5 are observed for GRDs between 0.2 and 0.4 m/lp. Based on the Rayleigh criterion of a minimum 20% contrast, the measurements demonstrate that the system can achieve a minimum NIIRS-6 imaging performance at a 1500 ft. standoff on-axis.

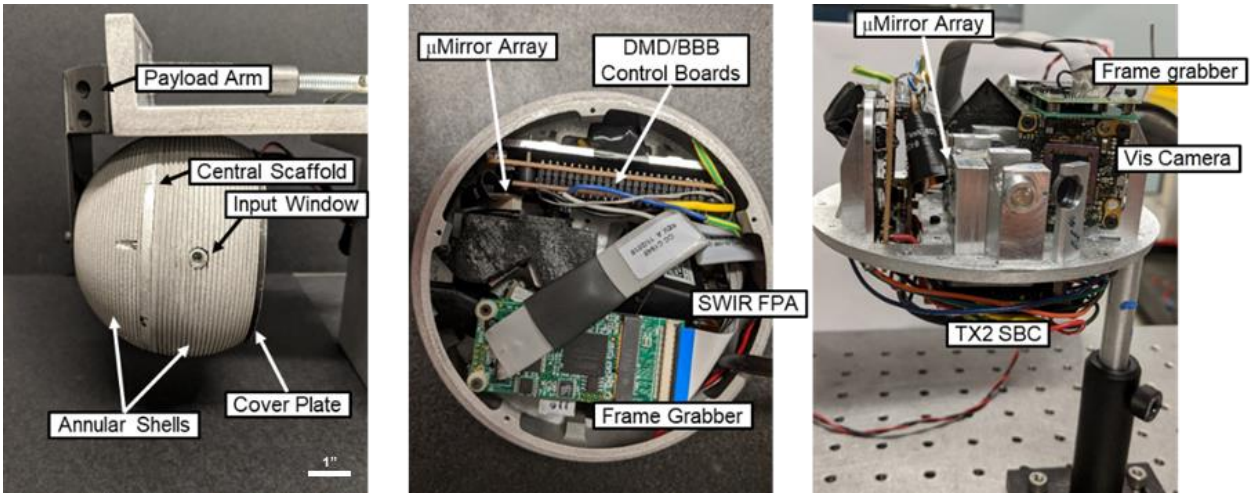

Figure 5: Assembled sensor.

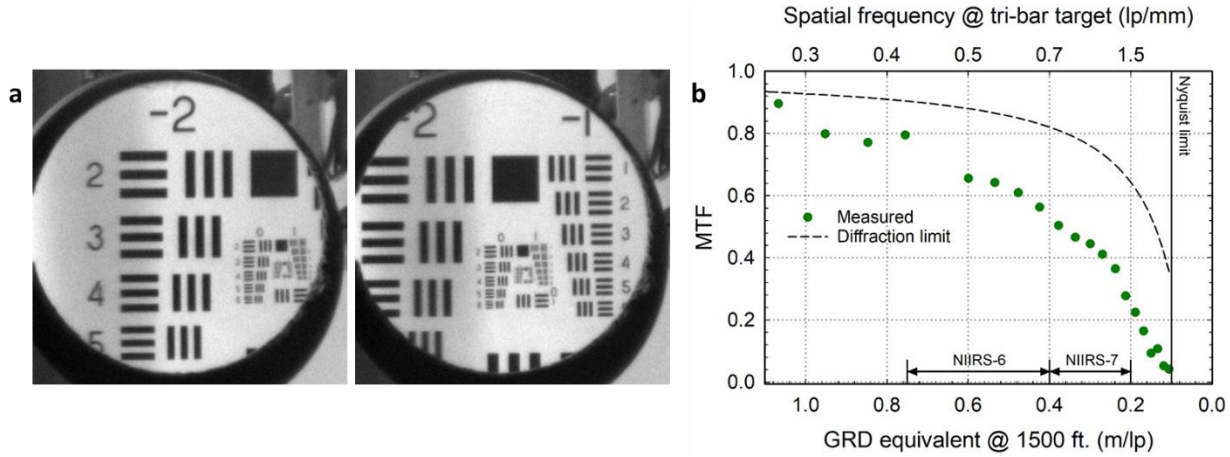

Figure 6. (a) FMV-acquired images of a USAF 1951 tribar target, (b) Measured (solid green circles) and calculated diffraction limited (dashed black line) MTF as a function of GRD equivalent at a 1500 ft. slant range. Associated bar target spatial frequencies are shown on the upper x-axis.

3.3 HSI performance characterization

The HSI spectrometer was functionally tested using a mercury-neon (HgNe) calibration lamp coupled with an integrating sphere. The lamp output has a rich spectrum in the 900-1600 nm spectral range, making it ideal for performance evaluation. Additionally, coupling with the integrating sphere results in uniform spectral radiance on the sensor's fore-optic that fills the etendue of the spectrometer. The resultant images can therefore be used to characterize the system for spectral dispersion, resolution, keystone and smile. Figure 7 shows a picture of the test assembly.

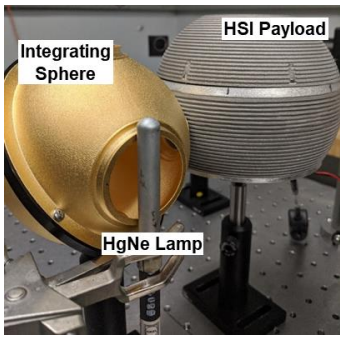

Figure 7: Spectrometer functional test assembly.

3.3.1 Spectral resolution and dispersion

Figure 8 shows the HSI-acquired images of the HgNe pen lamp for an (a) on- and (b) off-axis slit position. The horizontal and vertical axes represent spectral and spatial directions respectively. Numerical values on the axes indicate the pixel index, where each pixel is 37.5 µm. The spectral axis in the images below spans 6.125 mm on the InGaAs FPA. Four spectral lines, associated with prominent HgNe lines in the SWIR-1 band, are apparent in both images. The lines are assigned to the 1014, 1128, unresolved 1357/1367, and 1530 nm HgNe wavelengths and are indicated in the figure. Horizontal dashed green lines indicate differences in the vertical axis start/end pixels of the 1014 and 1530 nm lines – this will be discussed in more detail in the following sections.

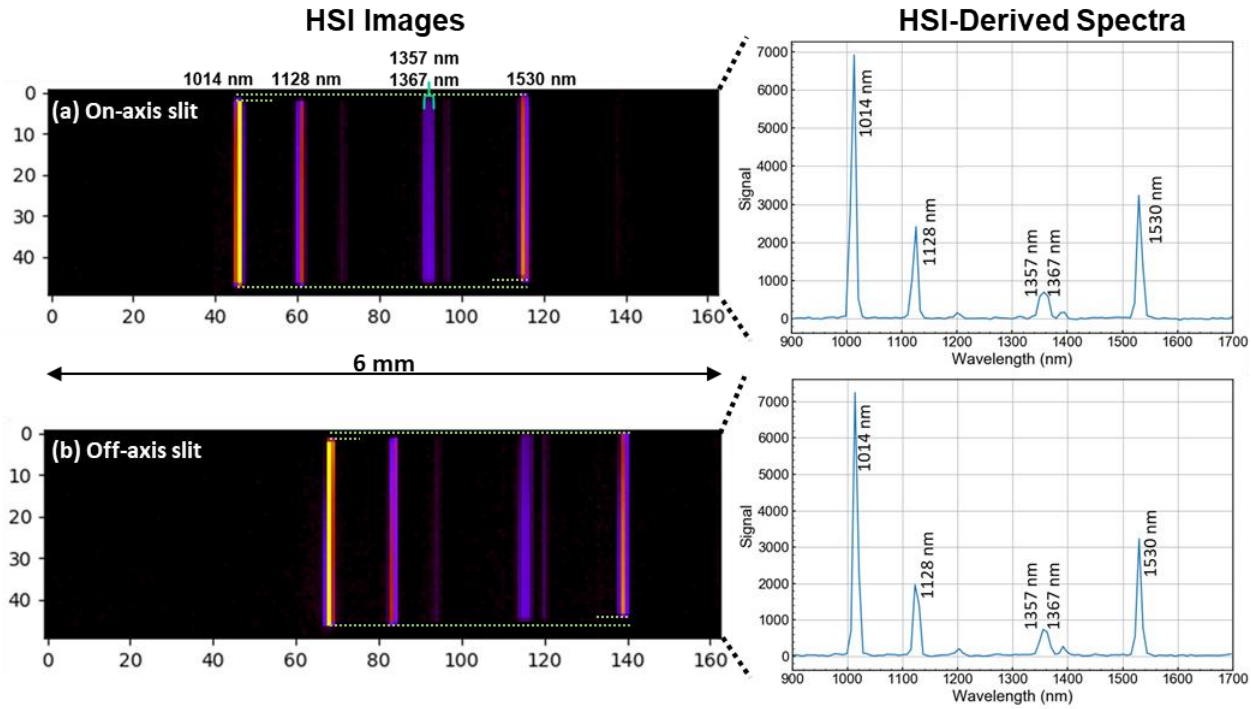

Figure 8: Representative hyperspectral image and associated calibrated spectrum of a HgNe pen lamp acquired by the HSI/FMV sensor for an (a) on- and (b) off-axis slit position. Horizontal green dashed lines are guides to the eye, indicating vertical spatial axis start and end positions of the 1014 and 1530 nm lines

The 1014 and 1530 nm lines were used to characterize the spectral dispersion of the system and generate associated pixel calibration curves. These are also shown in Figure 8. The calibration indicates a spectral dispersion of 7.5 nm/pixel. Calibration curves for each spectrometer slit were extracted in this manner and incorporated into the on-board SBC for automated data processing.

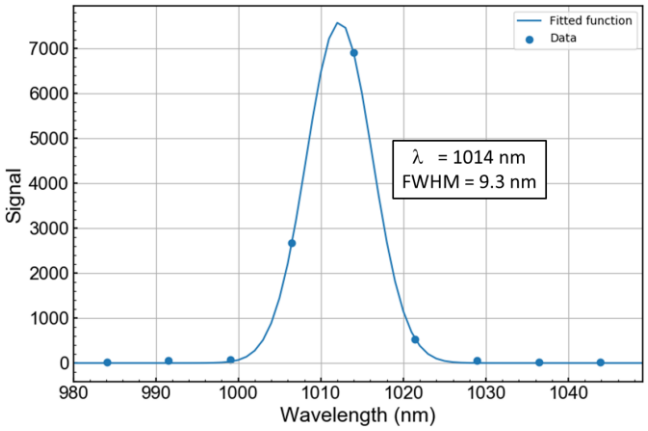

Figure 9: Representative example of the measured spectral resolution at the 1014 nm HgNe line.

The calibrated spectra were used to extract the spectral resolution of the HSI system by fitting the HgNe peaks to a Gaussian function where the width, σ, of the Gaussian fit yields FWHM ($=\sigma/2.355$), which in turn yields spectral resolution (=FWHM/0.88).[1] A representative example for the 1014 nm HgNe line is shown in Figure 9. Table 2 tabulates the measured FWHM and associated spectral resolution values for the 1014 and 1530 nm HgNe lines. The values indicate that the HSI system has spectral resolutions of ≤ 12 nm across its spectral and spatial range with an average value of 11 nm.

Table 2. Measured FWHM and spectral resolution for the HSI system.

Location	Measured FWHM at 1014 nm	Resolution at 1014 nm	Measured FWHM at 1530 nm	Resolution at 1530 nm
On Axis (0°)	9.3 nm	10.2 nm	10.3 nm	11.7 nm
Off Axis (2.5°)	9.1 nm	10.3 nm	9.5 nm	10.8 nm
Off Axis (-2.5°)	9.6 nm	10.9 nm	10.6 nm	12 nm

3.3.2 HSI Keystone

The horizontal dashed green lines in the HSI images in Figure 8 indicate an offset between the vertical axis start/end pixels of the 1014 and 1530 nm lines. This is a result of an asymmetric keystone or rotation in the HSI system. This effect was quantified by calculating edge positions of the 1014 and 1530 nm HgNe lines for on- and off-axis slit positions. Specifically, edge positions were determined by first performing a quadratic interpolation of the vertical line profile of the HgNe spectral lines. Next, the first derivative of the function was numerically calculated using a finite difference method. Specifically, the first derivative of a function, $f(x)$, can be approximated by

$$f'(x) \sim \frac{f(x+\Delta x) - f(x)}{\Delta x}, \tag{1}$$

when the interval, Δx, is small. An interval size of 0.0001 pixels was used to estimate the derivative of the interpolated function. Finally, pixel values for the maxima (minima) in the derivative curve (i.e. inflection points in the interpolated curve) were used to mark the rising (falling) edge of the spatial intensity profile. Figure 10 shows a representative example of this process. Specifically, Figure 10a shows the HSI image of the HgNe 1014 nm line and Figure 10b plots the intensity profile (open blue circles) along the dashed white line in Figure 10a. The solid blue curve is the interpolated function of the line profile. The vertical dashed line denote the edges calculated from the derivative of the interpolated function.

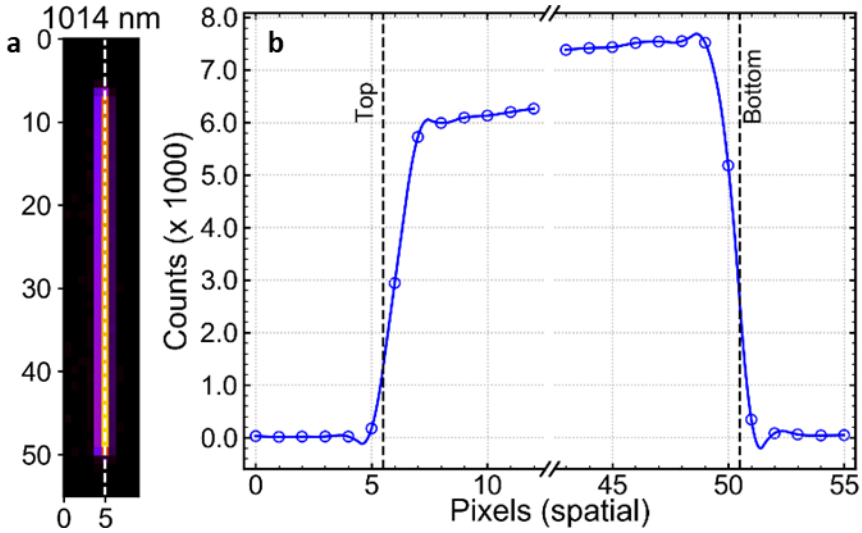

Figure 10: False color hyperspectral image of the 1014 nm HgNe line. (b) Spatial line profile (open blue circles) of (a) along the dashed white line with calculated top and bottom edge positions denoted as vertical dashed lines.

The calculated edge positions were used to quantify the rotation in the HSI images (θ). These are summarized in Table 3. The table shows that a maximum rotation of ~30 mrad is observed across the HSI image. Notably, θ values are not equal for the top and bottom edges for a given field point, indicating an asymmetry in the rotation or an asymmetric keystone effect. The keystone was further quantified through the difference in the width of the slit (Δw) between the 1014 and 1530 nm lines. This represents the change in the magnification along the spectral axis of the hyperspectral image. The table indicates that a maximum change of ±1 pixel in spatial extent is observed across the spectral range of the sensor. This is associated with a magnification change of only ±2.3%, highlighting the sensor's imaging performance.

Table 3: HSI system keystone summary.

Location		**θ (mrad)**	**Δw (pixels)**
On-axis (0°)	Top Bottom	14.5 29.0	1
Off-axis (−2.5°)	Top Bottom	29.0 29.0	0
Off-axis (+2.5°)	Top Bottom	14.5 0	-1

3.3.3 HSI smile

The spectral smile of the HSI payload was characterized by calculating the difference between the minimum and maximum spectral centroid for a given wavelength, as measured along a slit of the sensor. The centroid or center of mass of a spectrum ($x_{centroid}$) can be calculated using the following equation:

$$x_{centroid} = \frac{\sum_j (x_j * I_j)}{\sum_j I_j}. \quad (2)$$

Here x_j is the value of the j^{th} pixel along the spectral axis and I_j is its associated intensity. The centroid therefore essentially represents the weighted average along the spectral axis.

Figure 11 plots $x_{centroid}$ (open green circles) for each position along the vertical spatial axis of the hyperspectral image of the 1128 nm line in Figure 8a. The plot has a characteristic curved shape indicating the presence of spectral smile. This is highlighted by the dashed green line, which is a quadratic fit to the data and serves as a guide to the eye. The on-axis spectral smile of the sensor at 1128 nm is therefore the difference between the maximum and minimum $x_{centroid}$ values in Figure 11 and is equal to 0.23 pixels. We note that smile characterization in the literature uses the difference between the maximum and minimum of the quadratic fit.[2,3] This generally results in smaller values (0.10 pixels for the curve in Figure 11). However, we use the raw centroid data points to characterize the smile to obtain a conservative estimate.

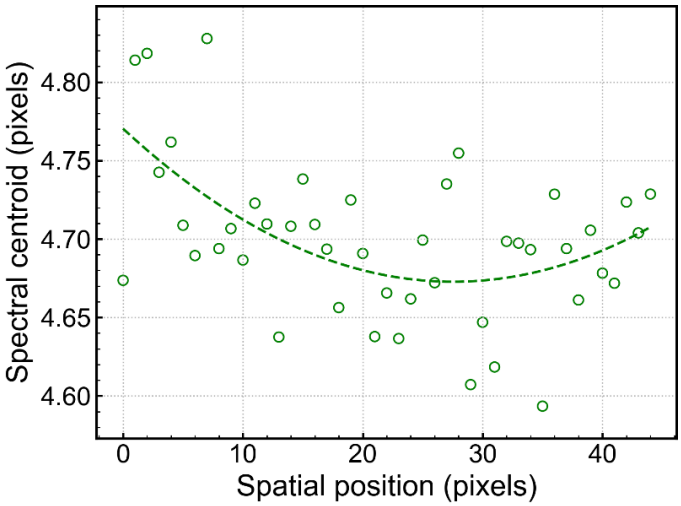

Figure 11: Measured spectral centroids (open green circles) for each pixel along the spatial axis for a HgNe 1128 nm line. The dashed green line is a quadratic fit and serves as a guide to the eye.

The spectral smile was similarly characterized for the 1013 and 1530 nm HgNe lines, for both on- and off-axis DMD slit positions. These values are listed in Table 4. Off-axis values are the average of two off-axis slit positions on either side of the center. The table indicates that the HSI sensor's smile is less than half a pixel across the sensor's spectral range. A wavelength-averaged smile of 0.17 pixels and 0.38 pixels is observed for on- and off-axis slit positions respectively, with an overall average of 0.28 pixels.

Table 4: Spectral smile for the hyperspectral sensor.

λ (nm)	Smile (pixels)	
	On-axis	Off-axis
1014	0.10	0.33
1128	0.23	0.43
1530	0.19	0.38
Average	0.17	0.38

3.4 HSI radiometric calibration and sensitivity

The HSI system was radiometrically calibrated using a calibrated 200 W Quartz Tungsten Halogen (QTH) lamp. The calibration configuration is shown in Figure 12. Specifically, the QTH lamp was placed 17 cm from the entrance port of an infragold integrating sphere. The spectral power density (*SPD*) entering the integrating sphere is given by:

$$SPD(\lambda) = H_{cal}(\lambda) * \left(\frac{D}{S}\right)^2 * A_{input} \quad (3)$$

where H_{cal} is the known calibrated QTH lamp spectral irradiance, D is the distance at which the QTH lamp is calibrated, S is the distance between the QTH lamp and the integrating sphere input port and A_{input} is the area of the integrating sphere input port. The sensor window was staring into the integrating sphere's exit port. The spectral radiance (L) incident on the sensor can be calculated using:

$$L(\lambda) = \frac{SPD(\lambda)}{\pi * A_{sphere}} * \frac{\rho(\lambda)}{1 - [\rho(\lambda) * (1 - f)]} \quad (4)$$

where A_{sphere} is the area associated with the integrating sphere diameter, ρ is the reflectance of infragold (94-96% in the 900-1600 nm spectral range) and f is the integrating sphere port fraction.

A "low" and "high" radiance was generated by using the QTH lamp with and without a 1 OD neutral density filter respectively, with a measured transmission spectrum. The filter, when used, was placed between the exit port of the integrating sphere and the sensor window, as indicated in Figure 12. The resultant high and low spectral radiance curves are shown in Figure 13a (dotted red and dashed blue lines respectively). Also shown is the typical spectral radiance expected to be incident on the HSI system (solid green line, based on sunlight reflecting from a 25% Lambertian reflector). It can be seen that the two radiances generated for the radiometric calibration span the range of expected values. HSI data cubes were subsequently acquired at each of these two radiances to generate a two-point radiometric calibration gain and offset.

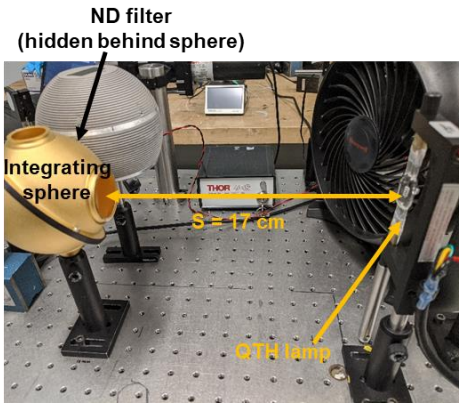

Figure 12: Radiometric calibration

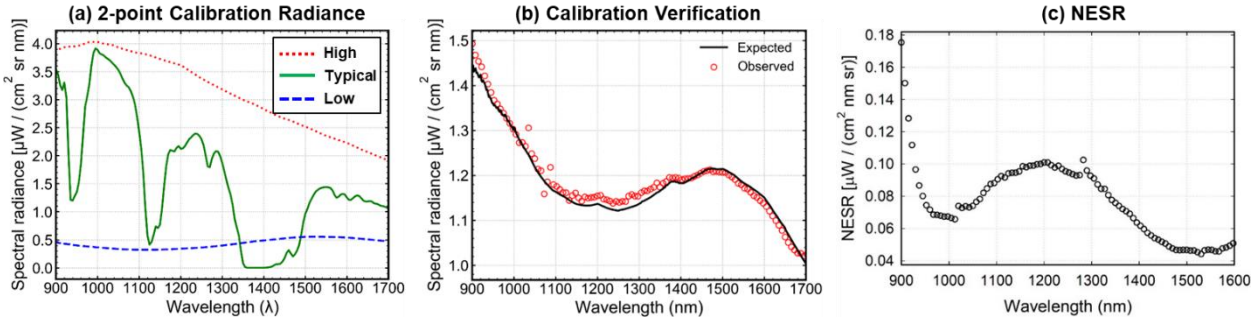

Figure 13: (a) Spectral radiance on the sensor window. The dotted red and dashed blue curves indicate the "high" and "low" radiances used for radiometric calibration. The solid green curve indicate the typical expected solar radiance on the sensor in deployment scenarios. (b) Expected (solid black curve) and measured (open red circles) spectral radiance from a QTH Lamp coupled with a 0.3 OD filter. (c) NESR of the HSI system.

The calibration was tested by generating an intermediate radiance curve using a 0.3 OD filter in the same configuration show in Figure 12, and comparing the measured with the expected spectrum. Figure 13b plots the expected (solid black curve) and measured (open red circles) for the intermediate radiance. The expected spectral radiance factors in the measured spectral profile of the filter used and is reflected in the shape of the curve. The measured radiance is the average across the sensor's field of view (FOV). It can be seen that the measured values are in close agreement with the expected radiance. A comparison of the measured and expected values indicate that the HSI system radiometric calibration is accurate to within 1.2% on an average, with a maximum deviation of 4.8% from expected values.

Finally, the sensitivity of the HSI system was measured by calculating the noise equivalent spectral radiance (NESR). Specifically, Figure 13c plots the NESR of the HSI system, defined as the standard deviation in 10 radiometrically calibrated spectra of the intermediate QTH radiance (0.3 OD filter), each averaged across the sensor's FOV. The plot shows that the HSI system NESR varies from ~40 to 180 μflicks, with a spectrally averaged value of ~100 μflicks. This NESR corresponds to a spectrally averaged SNR of 75 against typically expected spectral radiances on the sensor.

4. CAPABILITY DEMONSTRATION

4.1 Test set-up

The capabilities of the HSI/FMV system were demonstrated by testing the system against manmade targets using materials from an Air Force (AF)-provided reflectance spectra database of Home Depot materials. Specifically, 3 materials – Tyvek, Blue Cloth and Foamular – with reflectance features in the HSI system's spectral range, and sufficiently high expected contrast-to-noise ratios were selected. 2 × 4 ft.^{2} sheets of the three targets were mounted to a home-made bar target (16 × 4 ft.^{2}). Target materials were mounted on the bar target board such that each material was overlaid on a white bar and was spatially separated from other materials by a black bar of the board. A 1 ft.^{2} Spectralon target was also mounted

to the target board. The board was placed at a slant to the ground so as to expose a larger surface area to the incident sunlight. A picture of the target board is shown in Figure 14.

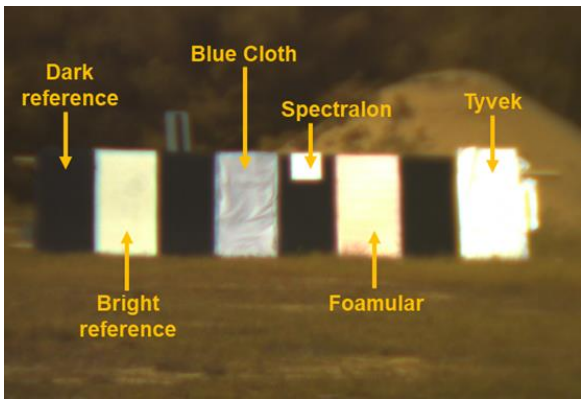

Figure 14: Target board used for outdoor tests.

The radiance from the target board was measured using the sensor at three different standoffs of 150, 200, and 310 ft. The data acquisition includes automated data processing on the on-board SBC (as described in Section 2). The HSI radiance cube was converted to a reflectance cube in post-processing using the Empirical Line Method (ELM) calibration.[4] Briefly, the ELM calibration uses the radiance from two or more reference objects in the scene with a known reflectance spectrum (typically both bright and dimly reflecting objects) to generate a reflectance vs. radiance calibration curve. This curve is then applied to the HSI cube to generate an associated reflectance cube. For the measurements collected, the white and black bars of the bar target not covered by the Home Depot materials were selected as the bright and dark reference materials to generate a 2-point ELM calibration curve. The Spectralon target was also used as a third reference when allowed by the sensor standoff.

4.2 Hyperspectral reflectance measurements

Figure 15(a) and (b) show the sensor acquired FMV and false-colored radiometrically calibrated broadband SWIR image of the target board, taken from a 150 ft. standoff. The 13 ft. HSI FOV at this standoff is smaller than the full 16 ft. span of the target board. However, all three Home Depot targets as well as a part of a white reference board is visible and clearly discernible in the SWIR image. Figure 16(a), (b), and (c) plot the resultant reflectance spectra of Blue Cloth, Foamular and Tyvek respectively, averaged across a 4×4 pixel area on the targets from a single HSI cube. Reflectance spectra were generated using the black and white bars, and the spectralon as ELM references. The symbols denote measured values and dashed black lines are the associated library spectra of each of the targets. Solid lines serve as guides to the eye and are derived from a Savitsky-Golay fit to the measured data. The break in the measured values between 1350-1450 nm arises from the breakdown in the ELM calibration curve at the third atmospheric water absorption band due to the near-zero radiance from all targets.

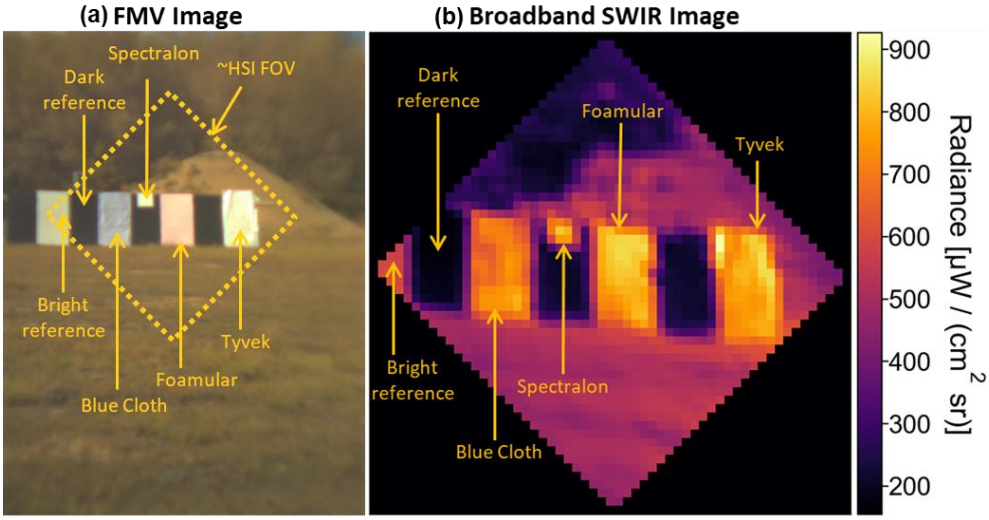

Figure 15: (a) FMV and (b) reconstructed broadband SWIR image of the target board from a 150 ft. standoff by the HSI/FMV sensor.

It can be seen from the plots in Figure 16 that measured and reference spectra of Blue Cloth and Tyvek are in good qualitative and quantitative agreement with the associated library reference spectra. The reflectance values of Foamular are higher than associated reference values, and in fact higher than 1. We attribute this observation to the glossy nature of Foamular's surface which generates significant specular reflection. However, the prominent Foamular peak at ~1150 nm is still evident in the measured spectrum and is highlighted by the vertical black dash-dotted line. Similar results were observed

for measurements at larger 200 and 310 ft. standoffs (data not shown). The HSI system is therefore able to reproduce reflectance spectra of materials with high fidelity.

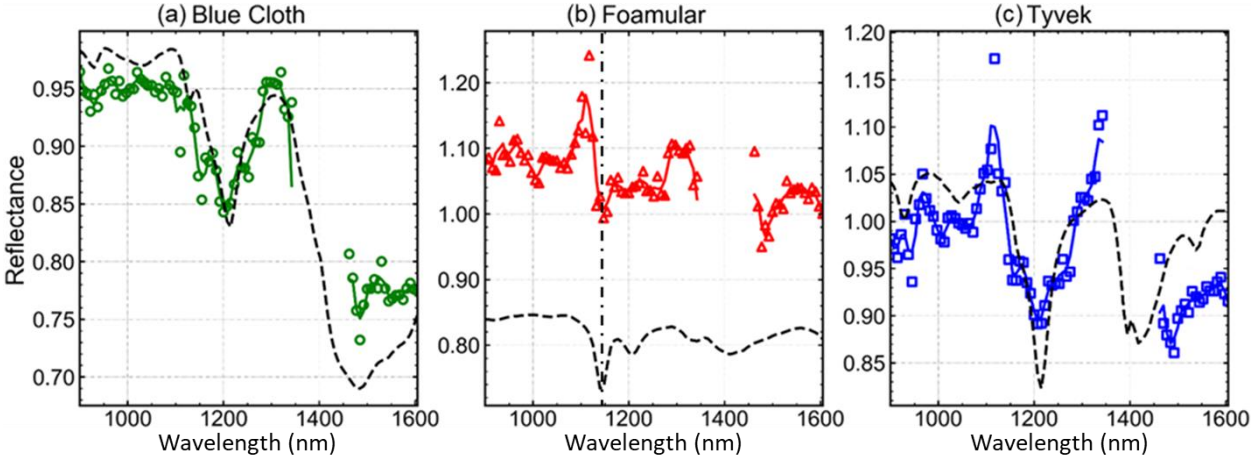

Figure 16: Measured reflectance spectra of (a) Blue Cloth, (b) Foamular and (c) Tyvek, averaged across a 4×4 pixel area in a single HSI cube acquired at a 150 ft. standoff. Symbols denote measured reflectance values while dashed lines denote library spectra. Solid lines are guides to the eye and derived from a Savitsky-Golay fit to the measured data. The vertical dash-dotted black line indicates the location of the prominent Foamular spectral feature at ~1150 nm.

4.3 Target detection

The utility of the HSI data product was demonstrated by applying spectral detection algorithms to the resultant reflectance cubes from the outdoor measurements. All spectra from the Home Depot material reflectance database (AF-provided) were convolved to the spectral resolution of the HSI system and used as library spectra for the detection algorithms. The algorithm was a combination of Spectral Angle Mapper (SAM), a match filter, and a spatial filter. If the spectrum from a given pixel in the reflectance cube had both SAM- and match filter scores against a library spectrum above pre-defined thresholds, the pixels was marked with a positive detection. The spatial filter applied a morphological filter (binary erosion and dilation) to the resultant detection map to minimize popcorn false alarms in the cube.

Figure 17 and Figure 18 shows the detection maps from HSI measurements at 200 and 310 ft. standoffs respectively, super-imposed on the broadband SWIR image of the scene, against (a) Blue Cloth, (b) Foamular and (c) Tyvek. Pixels marked red denote positive detections against the associated material. It can be seen that while there are a few false alarms against other targets (due to a high degree of spectral similarity), the algorithm always generates positive detections against each of the three materials at their respective location within the scene. Moreover, positive detections are observed on a majority of the pixels on the each of the three targets. These results therefore demonstrate the functionality of the HSI system towards manmade target detection applications.

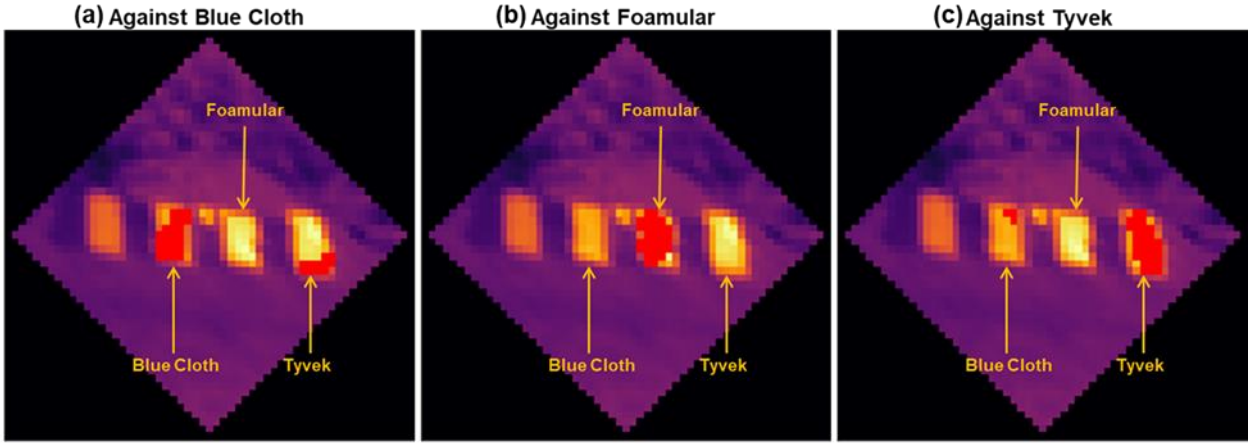

Figure 17: Detection maps generated with the measured 200 ft. standoff reflectance cube against (a) Blue Cloth, (b) Foamular and (c) Tyvek.

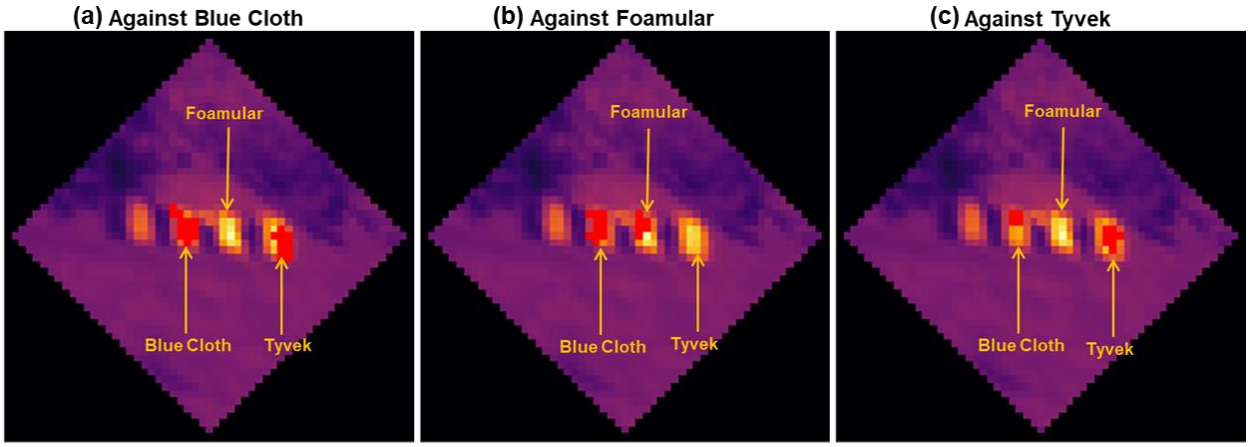

Figure 18: Detection maps generated with the measured 310 ft. standoff reflectance cube against (a) Blue Cloth, (b) Foamular and (c) Tyvek.

5. CONCLUSION

The work described here demonstrates the utility of PSI's fieldable compact HSI/FMV sensor. The system has been extensively characterized in laboratory settings for imaging and spectral performance to ensure compliance with design parameters. The sensor has been evaluated in outdoor environments and can successfully reproduce reflectance spectral of manmade targets placed in the sensor's FOV with high fidelity. Additionally, spectral correlation algorithms applied to the measured data products have demonstrated the detection of the target objects, demonstrating the utility of the sensor data product. The ultra-compact form factor and compatibility with gimbal based deployment makes the sensor well suited for diverse hyperspectral imaging based applications.

ACKNOWLEDGEMENT OF SUPPORT AND DISCLAIMER

This material is based upon work supported by United States Air Force under Contract Number FA8650-17-P-1186 and FA8650-19-C-1006.[5,6] Any opinions, findings and conclusions or recommendations expressed in this material are those of the author(s) and do not necessarily reflect the views of United States Air Force.

REFERENCES

[1] Griffiths, P., de Haseth, J.A., "Fourier Transform Infrared Spectroscopy", John Wiley & Sons, Inc., New Jersey, 16 (2006).
[2] Mouroulis, P., McKerns, M.M. "Pushbroom imaging spectrometer with high spectroscopic data fidelity: experimental demonstration," Opt. Eng., 39, 808-816 (2000).
[3] Hong, J., Kim, Y., Choi, B., Hwang, S., Jeong D., Lee, J.H., Kim, Y., Kim, H., "Efficient method to measure the spectral distortions using periodically distributed slit in hyperspectral imager," Opt. Express, 25, 20340 (2017).
[4] Smith, G.M., Milton, E.J., "The use of the empirical line method to calibrate remotely sensed data to reflectance", Int. J. Remote Sens., 20, 2653–2662 (1999).
[5] Giblin, J.P., "Compact Gimbaled Broadband Hyperspectral Imaging System", Final Report prepared for AFRL under Contract No. FA8650-17-P-1186, AFRL-RY-WP-TR-2018-0064 (2018).
[6] Giblin, J.P., Chatterjee, R., "Compact Gimbaled Broadband Hyperspectral Imaging System", Final Report prepared for AFRL under Contract No. FA8650-19-C-1006, AFRL-RY-WP-TR-2021-0078 (2021).